

Estimating the Feasibility of Probing the Epoch of Reionization with the 21cm-Ly α Cross-Power Spectrum

Prepared for:

Drs. Daniel Jacobs (Director), Judd Bowman, & Alexander Van Engelen
Arizona State University
School of Earth and Space Exploration

Prepared By:

Tyler Cox
Arizona State University
School of Earth and Space Exploration
Astrophysics Senior Thesis
December 5th, 2019

Abstract

One of the primary goals of astrophysics is the observation of the Epoch of Reionization. The Epoch of Reionization (EoR) is a period in the history of the universe during which the first luminous sources (stars, galaxies, etc.) formed and ionized the neutral gas around them. Despite best efforts of observations of this period, the process by which the universe transitioned from neutral to ionized is still largely a mystery. Next-generation reionization-era experiments such as the Hydrogen of Epoch of Reionization Array (HERA) and the Spectro-Photometer for the History of the Universe, Epoch of Reionization, and Ices Explorer (SPHEREx) look to independently probe the EoR by mapping the intensity of 21 cm and Lyman- α fluctuations respectively. While each instrument has the sensitivity to measure EoR fluctuations, bright radio foregrounds and low redshift H α interlopers make each of these measurements challenging. In addition, degeneracies in cosmological parameter estimates from each of these measurements make their interpretation challenging. Cross-correlation of these signals looks to be a promising way to reduce systematics from each instrument, provide an independent confirmation on the progression of reionization, and tighten constraints on cosmological parameter estimates. In this paper, I present estimates on the feasibility of detecting the 21 cm-Ly α cross-power spectrum as measured by HERA and SPHEREx. Using the reionization-era modeling code, 21CMFAST, I simulate 21 cm and Ly α fluctuations and show that HERA and SPHEREx has the ability to measure the cross-power spectrum at intermediate to large scales assuming reasonable estimates of the thermal noise contribution from both instruments. In future work, this technique will be used to put constraints on cosmological parameters and compared estimates made using the 21 cm and Ly α power spectra alone.

Contents

I. Contents	ii
II. List of Figures	iii
1 Introduction	1
1.1 The Early Universe	1
1.2 The Epoch of Reionization	2
1.3 The Hydrogen Epoch of Reionization Array	3
1.4 SPHEREx: an All-Sky Spectral Survey	5
1.5 Synergies Between Experiments	6
2. Modeling 21 cm and Lyα Fluctuations	10
2.1. 21 cm Fluctuations	10
2.2. Ly α Fluctuations	11
2.2.1 Ly α Emitters	12
2.2.2 Ionized IGM	14
2.2.3 Ly α Attenuation	16
3. Cross-Correlation Studies	20
3.1. Cross-Power Spectrum	20
3.2. Observational Uncertainties	23
3.3. Foreground Contamination	28
4. Conclusions	33
References	35

List of Figures

1.	Epoch of Reionization Timeline	1
2.	Reionization Constraints	4
3.	Spin-Flip Transition of Neutral Hydrogen	5
4.	Redshift and Resolution Coverage of Intensity Mapping Experiments	6
5.	HERA Image and Layout	7
6.	SPHEREx Instrument	8
7.	Simulated 21cm and Ly α emission	17
8.	21 cm Power Spectrum	21
9.	Ly α Power Spectrum	22
10.	21 cm-Ly α Cross-Power Spectrum	23
11.	Cross-Correlation Coefficient	24
12.	Cross-Power Spectrum Error Budget	27
13.	Foreground Wedge	29
14.	Optimistic vs. Moderate Foreground Treatment	31
15.	Cross-Power Spectrum Signal-to-Noise	32

Acknowledgements

First and foremost, I would like to thank the research advisors I've had since I've joined the Low-Frequency Cosmology Lab (in no particular order), Adam Beardsley, Judd Bowman, and Danny Jacobs. I am incredibly appreciative of your mentorship, advice, and support that you've provided over these past two years and so grateful for the opportunity that you've given me to work with the HERA team. Thank you to my third committee member, Alex Van Engelen, for enthusiastically agreeing to sit on my committee despite the late notice. I would also like to thank my friends, fellow students, and members of the Low-Frequency Cosmology Lab. In particular, I would like to thank Shane Bechtel, Lily Whitler, and Samuel Nigh for their support and friendship. They have all greatly enhanced my time here at ASU. Finally, I would like to send a heartfelt thank you to my parents and sister for their constant love and encouragement.

1 Introduction

1.1 The Early Universe

Immediately following the Big Bang, the Universe was primarily composed of a hot plasma of fundamental particles. In its early state, it was too hot and dense to form the atoms that comprise the complex structures that we observe today. Photons that were emitted during this early period scattered off free particles, leaving the Universe opaque to electromagnetic radiation. This lasted until roughly 400,000 years after the Big Bang, at which time the Universe had expanded and cooled sufficiently for electrons to bind to atomic nuclei, forming the first atoms of hydrogen and helium. Once formed, photons were able to freely propagate through the intergalactic medium (IGM). Today, we observe this as the cosmic microwave background radiation (CMB).

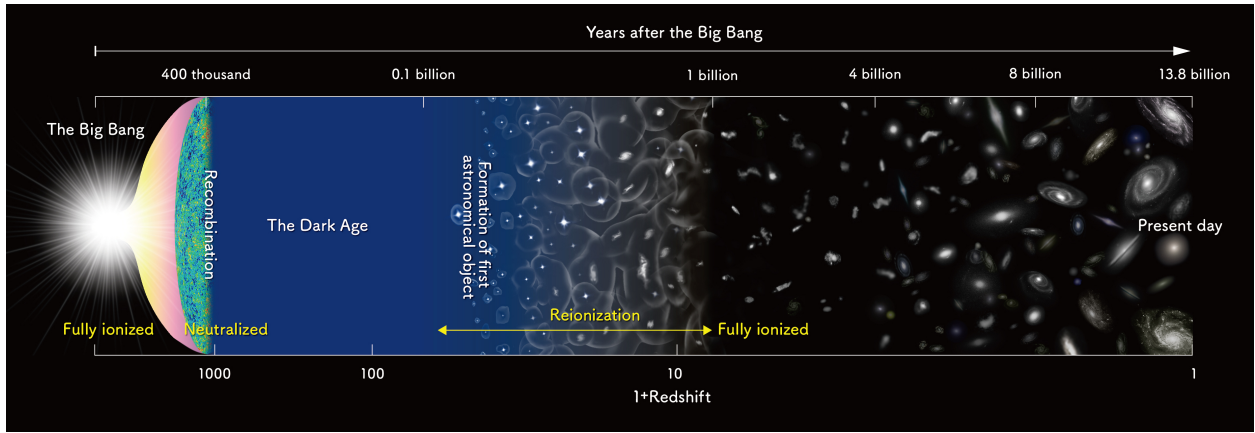


Figure 1. Timeline of the history of the universe from its formation (left) to present day (right).

Following this recombination of matter, the universe was largely neutral and stationary. Stars had not yet formed and the only emission detectable from this period originated from neutral hydrogen. This period, called the Cosmic Dark Ages, lasted until roughly a few hundred millions after the Big Bang, at which time the overdensities observed in the CMB

gravitationally collapsed to form the first luminous sources. Emitting ultraviolet (UV) radiation, these first stars and galaxies began ionizing the neutral gas around them. This period of time between the emergence of the first luminous sources and the ionization of the neutral gas between them, called the Epoch of Reionization (EoR), is believed to have lasted until around a billion years after the Big Bang.

Today, astronomers routinely observe high-redshift galaxies, allowing us to understand the evolution of galaxies following the end of reionization to present day. However, little is known about the timeline of reionization or the formation of objects that drove it. Studying the EoR provides us the opportunity to establish a bridge between the CMB and the structures we observe today, as well as provide insight to what the first luminous objects were like and how they formed.

1.2 The Epoch of Reionization

While modeling the Dark Ages is quite feasible given a few simple parameters and initial conditions set by the CMB, developing an accurate model of the EoR is quite difficult to do given its non-linear nature. A picture of reionization has unfolded giving us some insight into how reionization progressed. When the first luminous sources formed from gravitational collapse of overdense regions, they began producing UV photons which ionized the neutral gas in the IGM immediately around them. This ionized gas, now transparent to UV radiation, formed “bubbles” of material around these early galaxies. As these sources grew and others formed, ionizing radiation continued to pour into the IGM, causing these bubbles to grow and overlap with ionized bubbles surrounding neighboring sources. This progressed until all bubbles surrounding these early sources overlapped, leaving only trace amounts of neutral hydrogen within galaxies. This complete ionization of hydrogen in the IGM is what marked the end of reionization.

This general picture of reionization is relatively well accepted, but the details are largely unconstrained and leave many questions unanswered. The beginning of reionization, the

time it took the first luminous sources to fully ionize the IGM, and size and growth rate of early ionized bubbles are open questions which are sought to be answered. If we are able to answer these questions, we also have the ability to shed light on more fundamental areas of astrophysics, such as what the first luminous objects were like and how they formed.

While current measurements of the EoR are slim, there are a few studies that allow us to constrain the progress of reionization. Measurements of the polarization of the CMB can help place some restriction on the timing of reionization. By assuming reionization was instantaneous, the WMAP and Planck CMB probes used the optical depth of the CMB to infer a reionization redshift of $z \approx 8.8$. In addition, high-redshift quasar studies provide insight to when reionization likely came to a close. Using observations of the Gunn-Peterson trough, [Fan et al. \(2006\)](#) found that reionization concluded no later than $z \approx 6$. This technique will be used in future experiments, namely with the James Webb Space Telescope, to further constrain the neutral fraction of the IGM across cosmic time. The most up to date constraints on reionization including Planck and high-redshift galaxy measurements can be found in Figure 2.

In addition to CMB and high-redshift quasar measurements, other techniques are being developed to understand the progression of reionization. In particular, spectral line intensity mapping looks to be promising method of studying the EoR by constructing three dimensional maps of the universe using well-known spectral lines ([21 cm](#), Ly α , CII, CO, etc.). The major advantage of this method is that these spectral lines are narrow and well understood so observed redshift maps directly translate to an observation of a specific cosmic time. This method promises to place some of the tightest constraints on reionization by capturing the behavior of the first luminous objects and the IGM on large scales.

1.3 The Hydrogen Epoch of Reionization Array

With an understanding of the EoR and the challenges of observing it, we turn to some of the intensity mapping experiments that look to constrain reionization. Several instruments, such the Low Frequency Array (LOFAR; [Yatawatta et al. \(2013\)](#)), the Donald C. Backer

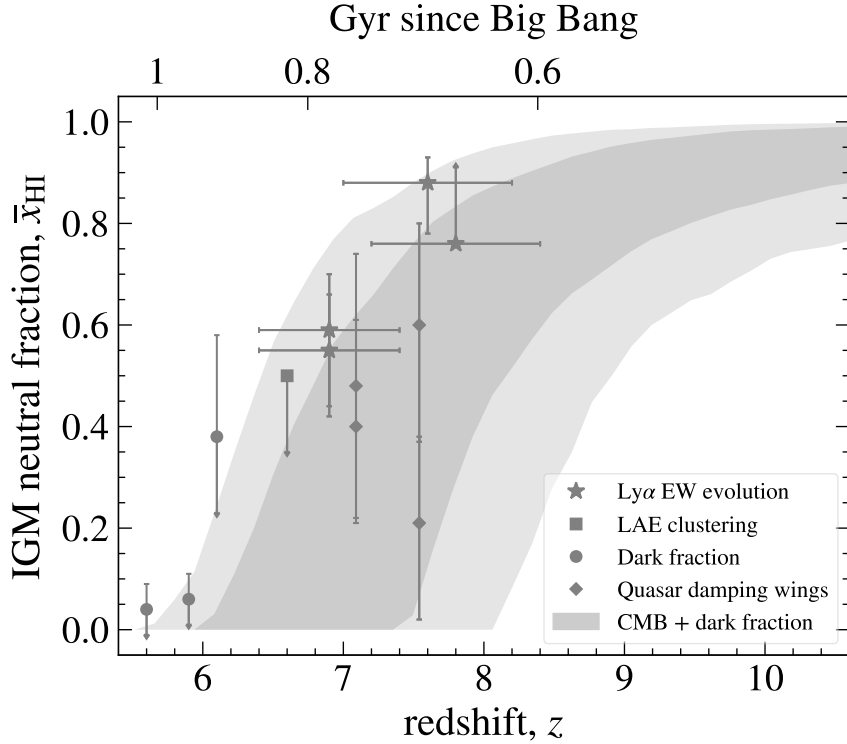


Figure 2. Constraints on reionization. Modified from [Whitler et al. \(2019\)](#)

Precision Array for Probing the Epoch of Reionization (PAPER; [Parsons et al. \(2010\)](#)), and the Murchison Widefield Array (MWA; [Tingay et al. \(2013\)](#)), have come online to help constrain reionization through the detection of neutral hydrogen emission between early stars and galaxies. Each of these approached the problem of detecting EoR fluctuations in their own way, but so far none have been successful at detecting the EoR signal. However, the lessons learned from each of these experiments have been used to help inform the construction of a next-generation 21 cm experiment, the Hydrogen Epoch of Reionization Array.

The Hydrogen Epoch of Reionization Array (HERA; [DeBoer et al. \(2017\)](#)) is a radio interferometer built in South Africa whose primary science goal is the study of large-scale structure through the power spectrum of the redshifted 21 cm line. When complete, HERA will be composed of a total of 350, 14-meter dishes, 320 of which will be tightly compacted in a hexagonal core with the remaining 30 placed outside the core to increase its imaging capabilities (Figure 5). This dense arrangement of dishes was designed specifically to avoid

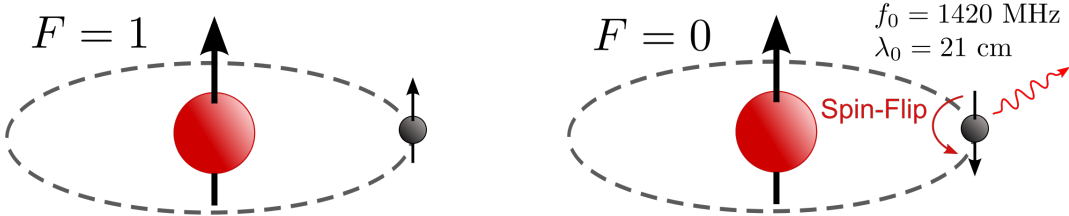


Figure 3. A depiction of the spin-flip transition of neutral hydrogen. Initially, the spin of the proton and electron are parallel and oriented in the same direction. The transition occurs when the electron’s spin spontaneously flips from the higher energy parallel alignment to the lower energy anti-parallel alignment, releasing a photon with a wavelength of 21 cm.

bright radio foregrounds 4-5 orders of magnitude brighter than the cosmological 21 cm signal. With a greater collecting area and a foreground avoidance strategy superior to previous experiments, HERA expects to measure EoR fluctuations at large-scales with high sensitivity and provide the first constraints on reionization-era astrophysical parameters using the 21 cm line. Construction is currently on-going to complete the array. It is estimated that HERA will be constructed and begin taking data with the full array in late 2020.

1.4 SPHEREx: an All-Sky Spectral Survey

In addition using the 21 cm line to characterize the EoR, intensity mapping of the Ly α transition of neutral hydrogen will provide a wealth of information about the state of reionization. The Ly α line has been shown to be a tracer of high-redshift galaxies and the bubble of ionized gas around them in [Silva et al. \(2013\)](#) and [Pullen et al. \(2014\)](#). A number of experiments look to probe reionization through the Ly α line, but the most prominent experiment of its kind planned for launch is that of the Spectro-Photometer for the History of the Universe, Epoch of Reionization, and Ices Explorer (SPHEREx), [Doré et al. \(2014\)](#).

SPHEREx is a near-infrared, space-based observatory whose primary science goal is to perform an all-sky survey in near-infrared bands of 450 million galaxies to constrain the physics of inflation using the large-scale structure of these galaxies. While not the primary goal of the mission, SPHEREx also looks to do intensity mapping of the Ly α line to study the origin and evolution of early galaxies. With a target launch date set for December

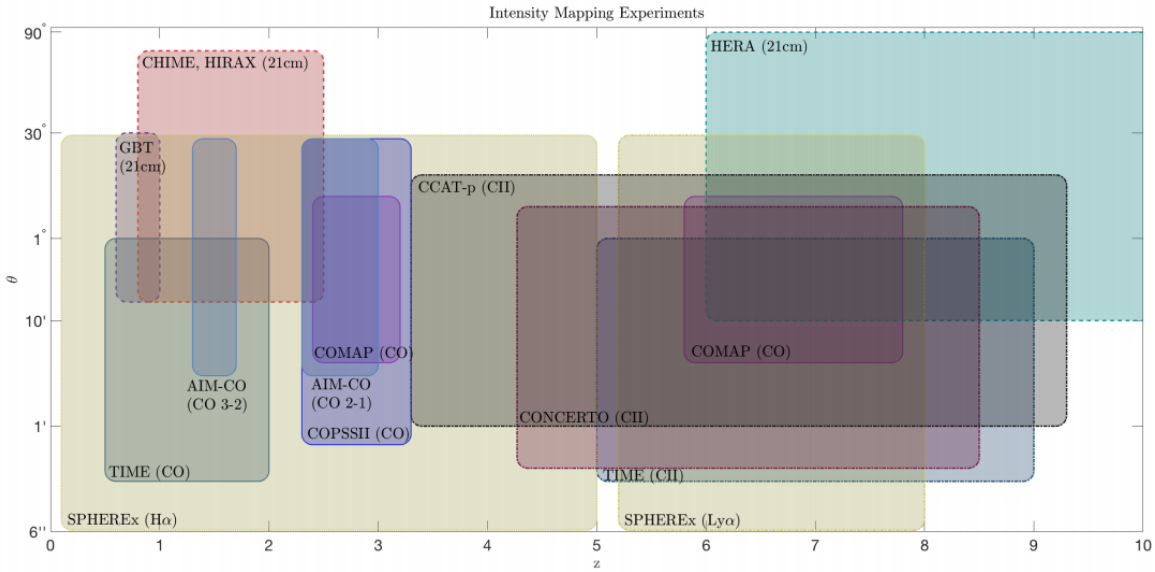


Figure 4. A figure representing the resolution, field of view, and redshift range of upcoming intensity mapping experiments.

2023, SPHEREx may provide the very first Ly α intensity mapping measurements during reionization. Given its sensitivity and frequency range, SPHEREx should be able to detect these EoR fluctuations over the redshift range $z \approx 6 - 8$.

1.5 Synergies Between Experiments

One particularly interesting area of study is that of synergies between experiments studying the reionization. As mentioned in previous sections, both HERA and SPHEREx have the potential to detect fluctuations during reionization. HERA will measure emission from neutral gas between early galaxies, while SPHEREx will study the ionized bubbles that the neutral gas surrounds. By combining measurements from HERA and SPHEREx, we have the potential to trace the entire IGM, neutral and ionized, providing more information on the progression of reionization than either measurement will be able to alone. Specifically, the cross-power spectrum and cross-correlation coefficients seem to very promising tools for understanding the reionization. Given that 21 cm emission traces the neutral medium and Ly α observes the ionized medium, cross-correlating these should produce a strong anti-

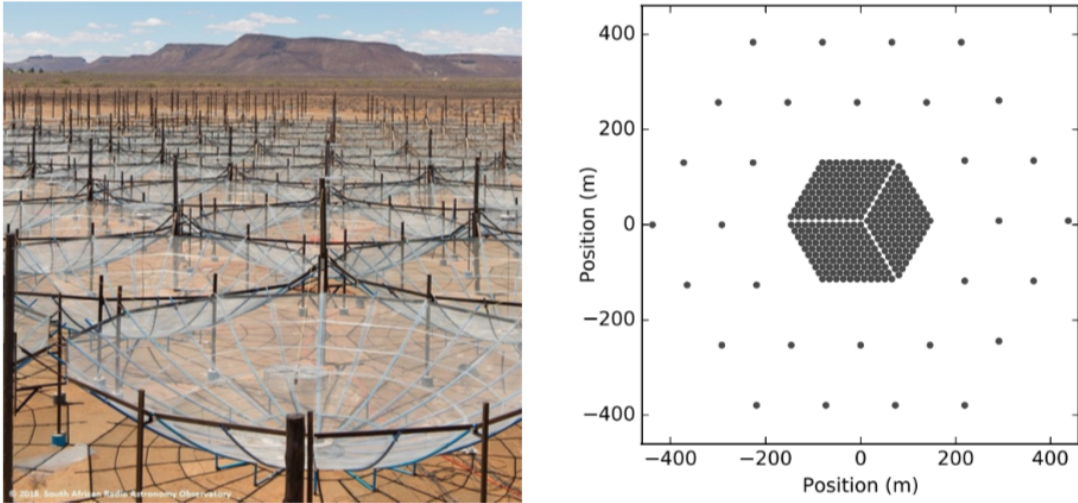


Figure 5. Left: An image of HERA as of late 2017. Right: A map of the full layout of HERA. The final array will contain a total of 350, 14 m dishes.

correlation on large spatial scales, where emission from these lines are completely separate, that smoothly transitions to no correlation on small spatial scales, where either only 21 cm or Ly α will be observed.

Cross-correlation of reionization-era measurements is proven to be feasible and useful for understanding the progression of the EoR. In [Hutter et al. \(2017\)](#), it was found that negative correlation appears when cross-correlating 21 cm and Ly α fluctuations that help break down degeneracies in parameter estimates that show up in estimates with 21 cm and Ly α measurements alone. Additionally, [Sobacchi et al. \(2016\)](#) showed that cross-correlating 21 cm and Ly α emitters helps to improve constraints on mean neutral fraction estimates. This technique has accomplished been done in practice using the Greenbank Telescope cross-correlating with galaxy surveys at $z \approx 0.8$, but a comparable measurement has never been made at reionization-era redshifts.

Past papers have demonstrated the feasibility of making a detection of the reionization-era 21 cm-Ly α cross-power spectrum, but with instruments that may be a decade or more away from being constructed ([Hutter et al. \(2017\)](#), [Heneka et al. \(2017\)](#), [Kubota et al. \(2018\)](#)).

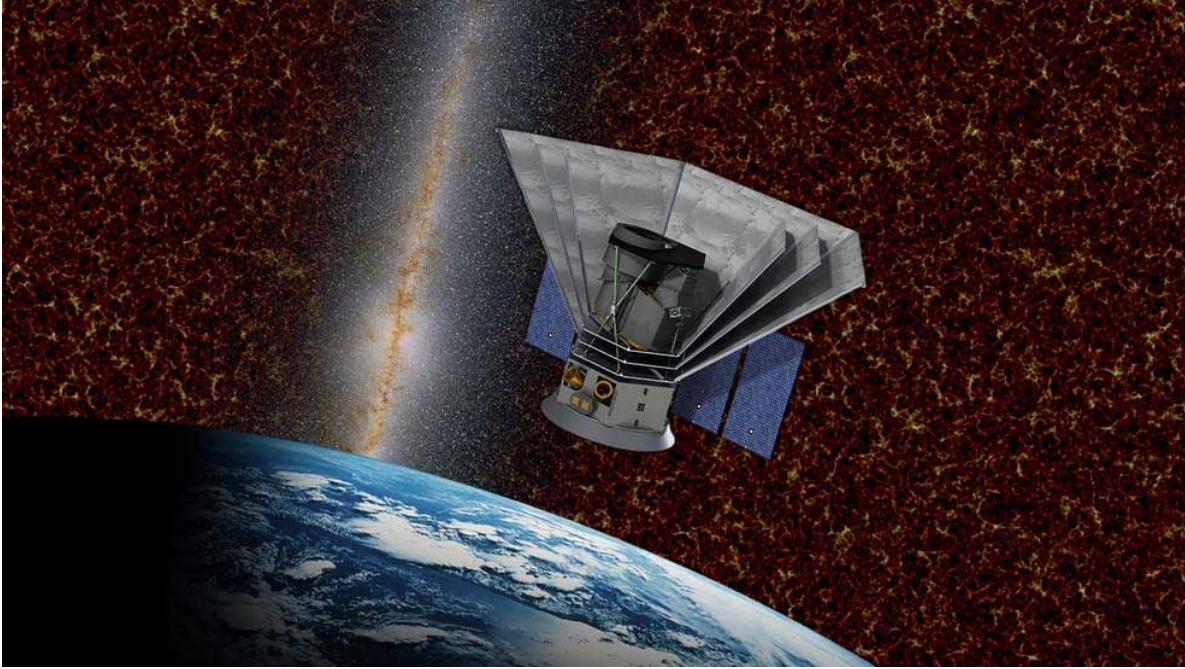


Figure 6. Simulated image of the SPHEREx probe in orbit.

While it is nearly certain that future experiments such as the Square Kilometer Array (SKA) and Cosmic Dawn Intensity Mapper (CDIM) will have the capability of making a detection of the cross-power spectrum, opportunities for its detection may be closer than past estimates suggest. With the construction of HERA’s 350 element array to be completed in 2020 and the launch SPHEREx targeted for the end of 2023, these two instruments have the potential to be the first to cross-correlate reionization-era intensity mapping measurements before the end of the next decade.

Both of these experiments have the potential to measure emission from $z \approx 6 - 8$ and are sensitive enough to detect the EoR on their own, but cross-correlation between these instruments is complicated by the fact that they measure different angular scales and are therefore sensitive to different spatial scales. They do overlap in the spatial scales that they measure (as can be seen in Figure 4), so a detection of the cross-power spectrum is technically possible given the amplitude of the signal and sensitivity that each instrument is able to achieve.

In the following section, I will estimate the amplitude of the cross-power spectrum and

calculate the cross-correlation coefficient by simulating 21 cm and Ly α fluctuation fields. I will then test the ability of HERA and SPHEREx to make a detection of the cross-power spectrum by estimating the noise on the cross-power spectrum using reasonable estimates of each instrument's spectral and spatial resolving power and taking into account sample variance, thermal noise variance, and two treatments of the 21 cm foregrounds.

2. Modeling 21 cm and Ly α Fluctuations

In this section, I will discuss the effort to model the 21 cm and Ly α cosmological signals that will be used for cross-correlation later in this work. A significant amount of research has gone into the modeling effort of both 21 cm and Ly α fluctuations during reionization. While N-body/radiative transfer codes accurately capture the physics of the evolution of galaxies and the IGM, they are computationally expensive and are difficult to extend to the large cosmological volumes that HERA and SPHEREx will attempt to observe. Semi-numerical simulators on the other hand are much more computationally efficient at modeling the large-scale evolution of the IGM and strongly agree with more numerically motivated simulators at the large scales that these intensity mapping experiments are concerned with. Additionally, computational efficiency is not only more convenient, but necessary for later parameter studies. For this work, I make use of the semi-numerical simulator, 21CMFAST ([Mesinger et al. \(2011\)](#)), to simulate 21 cm emission and to generate the density and ionization fields and halo catalogue necessary for the simulation of Ly α emission in later subsections.

Throughout this work, I assume a flat, Λ CDM cosmology using cosmological parameters consistent with [Planck Collaboration et al. \(2016\)](#) and astrophysical parameters defined in the 21CMFAST fiducial model. The physical comoving size of the simulation cubes was $200 \times 200 \times 200$ Mpc 3 with a voxel resolution of 256 voxels on a side.

2.1. 21 cm Fluctuations

In this subsection, I briefly describe the simulation of the 21 cm cosmological signal. As mentioned in the previously, 21CMFAST was written specifically to simulate the 21 cm signal. It does this by generating density, velocity, and ionization fields at $z \approx 35$ and evolving them through cosmic time. With these fields and the following expression, the brightness

temperature offset of the 21 cm signal can then be evaluated at a given redshift.

$$\begin{aligned}\delta T_b(z) &= \frac{T_S - T_\gamma}{1+z} \left(1 - e^{-\tau_{\nu_0}}\right) \\ &\approx 27x_{\text{HI}}(1 + \delta_{\text{nl}}) \left(\frac{H}{dv_r/dv + H}\right) \left(1 - \frac{T_\gamma}{T_S}\right) \\ &\quad \times \left(\frac{1+z}{10} \frac{0.15}{\Omega_M h^2}\right)^{1/2} \left(\frac{\Omega_b h^2}{0.023}\right) \text{ mK},\end{aligned}\quad (1)$$

In the equation above, T_S is the gas spin temperature, T_γ is the CMB temperature, τ_{ν_0} is the optical depth at 21cm frequency, $\delta_{\text{nl}} = \rho/\bar{\rho}_0 - 1$ is the non-linear density contrast, $H(z)$ is the Hubble parameter, dv_r/dr is the comoving gradient of the line of sight component of the comoving velocity, where all quantities are evaluated at redshift $z = \nu_0/\nu - 1$. The brightness temperature offset can then be converted to a fluctuation field for cross-correlation using the equation below,

$$\delta_{21}(\mathbf{x}, z) = \frac{\delta T_b(\mathbf{x}, z)}{\delta \bar{T}_b(z)} - 1, \quad (2)$$

where $\delta \bar{T}$ is the spatial average of the 21 cm brightness temperature offset $\delta T(\mathbf{x}, z)$. The simulated 21 cm brightness temperature offset field defined in Equation 1 can be seen in Figure 7.

2.2. Ly α Fluctuations

Here, I will describe the parameterization of Ly α emission during reionization. I adopt the technique developed in Silva et al. (2013) and first applied to 21CMFAST simulations in Heneka et al. (2017) for simulating Ly α intensity mapping measurements. While those works already provide in-depth descriptions of the relationships used to simulate Ly α emission, I will restate those methods in the following sections. Using this procedure, Ly α fluctuations can be modeled from two distinct sources. They are:

1. *Ly α Emitters (LAE):* This is emission that originates from within the virial radius Ly α -emitting galaxies themselves. The dominate components that contribute to emission within these galaxies are hydrogen recombinations and collisional excitation.

2. *Ionized Intergalactic Medium (IGM)*: This is emission that stems from the bubble of ionized gas that surround Ly α -emitting galaxies. In these ionized bubbles, recombinations of ionized hydrogen is the dominate contributor to Ly α emission.

In the following sections, I will describe the procedure for simulating Ly α emission from these two sources during reionization using 21CMFAST halo catalogues and kinetic gas temperature, non-linear density contrast, and ionization cubes.

2.2.1 Ly α Emitters

I start by describing the emission of EoR Ly α stemming from Ly α emitting galaxies. As mentioned above, the emission of Ly α photons in LAE's is a result of two dominant processes: the recombination of ionized hydrogen within the virial radius of the halos and collisional excitations of neutral hydrogen. [Silva et al. \(2013\)](#) also modeled two other contributions to Ly α emission within these halos but found them to be subdominant, so for this work I just focus on these two main sources. Both of these dominant sources of Ly α emission are closely related to star formation and therefore will be dependent star formation rate (SFR) of the LAEs, which is parameterized by their halo mass.

I'll begin by discussing Ly α emission stemming from recombinations of ionized hydrogen. The expression for the Ly α luminosity of a galaxy with mass, M , at redshift, z is defined as,

$$L_{\text{rec}}^{\text{gal}}(M, z) = E_{\text{Ly}\alpha} \dot{N}_{\text{Ly}\alpha}(M, z), \quad (3)$$

where I assume the emission of Ly α radiation at rest-frame frequency with energy $E_{\text{Ly}\alpha} = 13.6$ eV. The relationship above gives the luminosity of Ly α emission from galaxies by calculating the rate of Ly α photons being emitted and multiplying it by the energy of Ly α photons. The number of Ly α photons being emitted per second, $\dot{N}_{\text{Ly}\alpha}$, can be estimated using the relationship below,

$$\dot{N}_{\text{Ly}\alpha}(M, z) = A_{\text{He}} \dot{N}_{\text{ion}} f_{\text{rec}} f_{\text{Ly}\alpha} [1 - f_{\text{esc}}(M, z)]. \quad (4)$$

Here $A_{\text{He}} = (4 - Y_{\text{He}}) / (4 - 3Y_{\text{He}})$ (for helium mass fraction $Y_{\text{He}} = 0.24$) and the fraction of recombinations which result in the emission of a Ly α photon, $f_{\text{rec}} \approx 0.66$. The fraction of Ly α photons not absorbed by dust is parameterized in [Hayes et al. \(2011\)](#) by the expression,

$$f_{\text{Ly}\alpha} = C_{\text{dust}} \times 10^{-3} (1 + z)^{\zeta} \quad (5)$$

where $C_{\text{dust}} = 3.34$ and $\zeta = 2.57$. Below, the relationship for the escape fraction of Ly α radiation is given as,

$$f_{\text{esc}}(M, z) = \exp[-\alpha(z) M^{\beta(z)}], \quad (6)$$

where α and β are redshift dependent parameters defined in [Razoumov & Sommer-Larsen \(2010\)](#). The key relationship in this model is the star formation rate (SFR) which is parameterized by the mass of the halo,

$$\text{SFR} = 2.8 \times 10^{-28} \left(\frac{M}{M_{\odot}} \right)^a \left(1 + \frac{M}{c_1} \right)^b \left(1 + \frac{M}{c_2} \right)^d [M_{\odot} \text{ yr}^{-1}]. \quad (7)$$

In this relationship, $a = -0.94$, $b = -1.7$, $c_1 = 10^9 M_{\odot}$, $c_2 = 7 \times 10^{10} M_{\odot}$, and $d = -1.7$ are fitted parameters defined in ([Silva et al. \(2013\)](#)). Finally, the total number of ionizing photons is defined as $\dot{N}_{\text{ion}} = Q_{\text{ion}} \times \text{SFR}(M, z)$ where $Q_{\text{ion}} \approx 5.8 \times 10^{60} M_{\odot}^{-1}$ ([Schaerer \(2002\)](#)). The value for Q_{ion} was found by modeling stellar lifetimes and estimating the number of ionizing photons per unit time.

The other dominant contributor of Ly α emission in galaxies is excitation during hydrogen ionization. The Ly α luminosity in the interstellar medium due to these excitations is defined as,

$$L_{\text{exc}}^{\text{gal}}(M, z) = A_{\text{He}} f_{\text{Ly}\alpha} [1 - f_{\text{esc}}(M, z)] E_{\text{exc}} \dot{N}_{\text{ion}}, \quad (8)$$

where all terms have been previously defined, with the exception of $E_{\text{exc}} \approx 2.14\text{eV}$, which was determined by estimating the average ionizing photon energy for thermal equilibrium, $E_\nu = 21.4\text{ eV}$, ([Maraston \(2005\)](#)) and relating it to the energy emitted as Ly α radiation due to excitations, $E_{\text{exc}}/E_\nu \approx 0.1$ ([Gould & Weinberg \(1996\)](#)). With both dominant contributions to Ly α emission modeled, I assign a Ly α luminosity to each halo dependent on its mass using the parameterization above. These luminosities can then be converted to a surface brightness by dividing them by the simulation comoving voxel size and using the following expression,

$$I_\nu^{\text{gal}}(\mathbf{x}, z) = y(z) d_A^2(z) \frac{L^{\text{gal}}(\mathbf{x}, z)}{4\pi d_L^2}. \quad (9)$$

Here d_A is the comoving angular diameter distance, d_L is the luminosity distance, and $y(z) = \lambda_0(1+z)^2/H(z)$ (for the rest-frame wavelength of Ly α radiation, $\lambda_0 = 1216\text{ \AA}$). With these surface brightnesses calculated, a cube of Ly α emission from galaxies can then be constructed by adding the emission from galaxies to their cooresponding voxel position, \mathbf{x} . This produces a cube of Ly α emission from galaxies that is scaled by their masses and follows the spatial distribution of the halos. A slice of these simulation cubes across the redshift range of interest can be found in Figure 7.

2.2.2 Ionized IGM

In this subsection, I describe the Ly α emission from the ionized IGM. As mentioned at the beginning of this section, I focus on Ly α emission in the ionized IGM due to hydrogen recombinations. As with Ly α emitting galaxies, the ionized bubbles around galaxies also emit Ly α photons through recombinations of ionized hydrogen. The luminosity density of Ly α emission in some voxel of the simulation cubes can be defined using the following relationship,

$$l_{\text{rec}} = E_{\text{Ly}\alpha} f_{\text{rec}} \dot{n}_{\text{rec}}(\mathbf{x}, z), \quad (10)$$

where $E_{\text{Ly}\alpha}$ is the rest-frame energy of Ly α photons, f_{rec} is the fraction of recombinations that result in the emission of a Ly α photon, and \dot{n}_{rec} is the comoving number density of

recombinations occurring in the ionized IGM. The expression for the number density of recombinations reads as,

$$\dot{n}_{\text{rec}}(\mathbf{x}, z) = \alpha_A n_e(z) n_{\text{HII}}(z), \quad (11)$$

where $n_e = x_i(\mathbf{x}, z) n_b(\mathbf{x}, z)$, $n_{\text{HII}} = n_e (4 - 4Y_{\text{He}}) / (4 - 3Y_{\text{He}})$ and α_A is the comoving recombination coefficient. The comoving baryonic number density can be expressed using the relationship below,

$$n_b(\mathbf{x}, z) = \bar{n}_{b,0} (1+z)^3 [1 + \delta_{\text{nl}}(\mathbf{x}, z)], \quad (12)$$

where n_b is dependent on the non-linear density contrast, $\delta_{\text{nl}}(\mathbf{x}, z)$, and the present-day mean baryonic number density, $\bar{n}_{b,0} = 1.905 \times 10^{-7} \text{ cm}^{-3}$. Finally, the comoving recombination coefficient, α_A , is defined below,

$$\alpha_A \approx 4.2 \times 10^{-13} \left(T_K / 10^4 \text{ K} \right)^{-0.7} (1+z)^3 \left[\text{cm}^3 \text{ s}^{-1} \right]. \quad (13)$$

The comoving number density of recombinations, \dot{n}_{rec} , per pixel is simulated by using 21CMFAST to evolve the kinetic gas temperature $T_k(\mathbf{x}, z)$, comoving baryonic number density $n_b(\mathbf{x}, z)$, and the ionization fraction $x_i(\mathbf{x}, z)$ for each voxel in the simulation cube. With the number density of recombinations calculated in each voxel, the luminosity density of Ly α emission in the ionized IGM can be calculated and converted to a surface brightness using the following relationship,

$$I_{\nu}^{\text{rec}} = y(z) d_A^2(z) \frac{l_{\text{rec}}(\mathbf{x}, z)}{4\pi d_L^2(z)}. \quad (14)$$

In reality, Ly α emission from the ionized IGM also includes the scattered IGM Ly α background whose main contributors are X-ray and UV heating, as well as the scattering of Lyman-n photons emitted from galaxies by residual neutral hydrogen in the ionized IGM (Pritchard & Furlanetto (2007)). For this work, I chose to neglect the contribution from this Ly α background as its contribution is subdominant to hydrogen recombination in the ionized IGM (roughly half the mean surface brightness) and the galactic Ly α contribution

(about an order of magnitude lower) as found in [Silva et al. \(2013\)](#) and [Heneka et al. \(2017\)](#). Adding in the Ly α background contribution in the future should be trivial as 21cmFAST keeps track of this its emission when evolving the kinetic gas temperature and the ionization field. The surface brightness of Ly α emission due to this background, $J_\alpha(\mathbf{x}, z)$, can then be calculated using the following expression ([Silva et al. \(2013\)](#)):

$$I_\nu = \frac{6E_{\text{Ly}\alpha} d_A^2(z)}{(1+z)^2 d_L^2(z)} J_\alpha(\mathbf{x}, z). \quad (15)$$

With all of the components of Ly α emission during the EoR simulated and converted to surface brightnesses, I then calculate the fluctuation field of Ly α emission by summing over the individual contributions to Ly α emission from galaxies and the ionized IGM.

$$\delta I_\nu(\mathbf{x}, z) = \sum_i \frac{\nu I_{\nu,i}(\mathbf{x}, z)}{\nu \bar{I}_\nu(z)} - 1 \quad (16)$$

This expression will be used to calculate the Ly α auto-power spectrum and the 21 cm-Ly α cross-power spectrum in the following section. The slices through the simulated 21 cm and the various components of Ly α emission cubes are shown in Figure 7.

2.2.3 Ly α Attenuation

In order to more realistically estimate the observed Ly α emission from galaxies, attenuation of Ly α by the IGM needs to be taken into account. I use the expression below to calculate the Ly α luminosity from galaxies actually observed,

$$L_{\text{obs}}^{\text{gal}} = L^{\text{gal}} e^{-\tau_{\text{Ly}\alpha}}. \quad (17)$$

Here L^{gal} is the luminosity of Ly α emitting galaxies defined in the previous section and $\tau_{\text{Ly}\alpha}$ is the optical depth of Ly α emission at some redshift.

The general picture of the attenuation of Ly α radiation from galaxies is as follows: Ly α radiation is emitted by some source and as that radiation travels from the virial radius

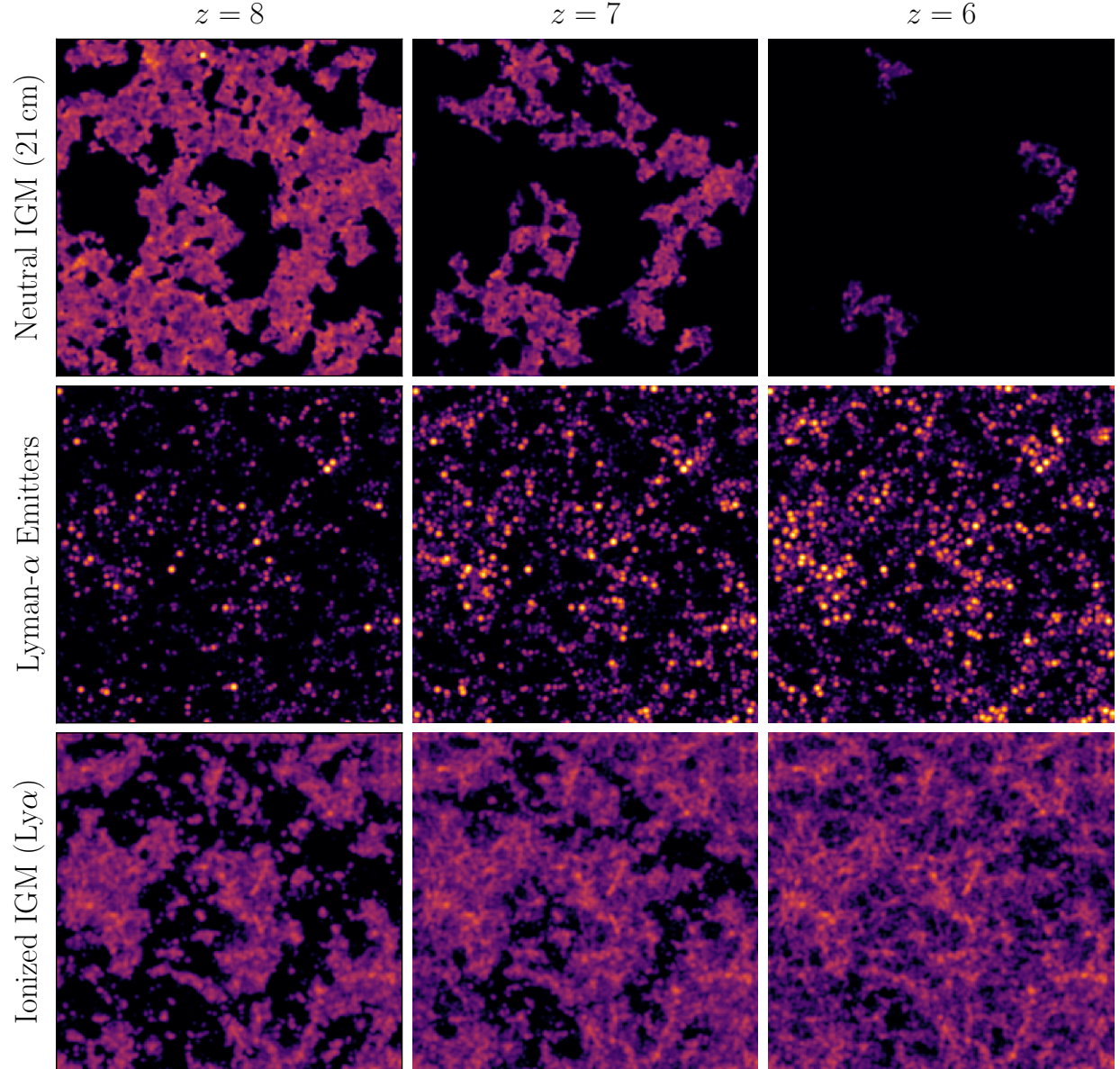


Figure 7. Slices through the simulated 21 cm brightness temperature offset, δT_b , Ly α emitter and ionized IGM cubes at $z = [6, 7, 8]$. Details on these simulations are described in Sections 2.1, 2.2.1, 2.2.2 respectively. The simulated box length is 200 Mpc on a side. These fluctuation fields are used in later sections (Section 3.1) to calculate the 21 cm-Ly α cross-power spectrum.

of that Ly α emitter to the edge of the ionized bubble, it is redshifted out of resonance and into the line damping wings, where it has a lower probability of being absorbed. As reionization progresses and the ionized bubbles around halos grow, the probability of Ly α being attenuated decreases given the fact that it redshifts more for reaching the neutral hydrogen. To simulate this behavior, I use a model for the optical depth of Ly α that is defined in Miralda-Escudé (1998). The key equation associated with this model is given by,

$$\tau_{\text{Ly}\alpha} = \tau_s \bar{x}_{\text{HI}} \left(\frac{2.02 \times 10^{-8}}{\pi} \right) \left(\frac{1+z_s}{1+z_{\text{obs}}} \right)^{1.5} \times \left[I \left(\frac{1+z_s}{1+z_{\text{obs}}} \right) - I \left(\frac{1+z_{\text{reion}}}{1+z_{\text{obs}}} \right) \right] \quad (18)$$

where z_s is the redshift of a Ly α emitting source, z_{obs} is the redshift of the observation, , and \bar{x}_{HI} , is the mean neutral fraction. This assumes that the optical line depth at Ly α line resonance, τ_s , can be approximated as

$$\tau_s \approx 6.45 \times 10^5 \left(\frac{\Omega_b h}{0.03} \right) \left(\frac{\Omega_m}{0.3} \right)^{-0.5} \left(\frac{1+z_s}{10} \right)^{1.5} \quad (19)$$

at high-redshifts for a source at some redshift, z_s , given present day, Ω_b , and Ω_m (Gunn & Peterson (1965), Barkana & Loeb (2001)). In the expression above, I is the helper function,

$$I(x) = \frac{x^{4.5}}{1-x} + \frac{9}{7}x^{3.5} + \frac{9}{5}x^{2.5} + 3x^{1.5} + 9x^{0.5} - 4.5 \log \left(\frac{1+x^{0.5}}{1-x^{0.5}} \right). \quad (20)$$

To calculate the difference between z_s and z_{obs} , I estimated the mean ionized bubble size at some z_{obs} by counting the number of voxels between each halo and the nearest voxel which contained neutral gas and averaging that value over all halos. I then scaled this value by the comoving voxel size to obtain an estimate on the mean ionized bubble size at z_{obs} . This was then converted to a z_s value using the relationship $z_s = z_{\text{obs}} - H(z_{\text{obs}})D/c$, where D is the

typical ionized bubble size. As expected, this model results in greater attenuation at high-redshifts and decreases as the ionized bubbles grow and the mean neutral fraction decreases. The effect of the attenuation resulted in Ly α transmission values of $e^{-\tau_{\text{Ly}\alpha}} \approx 0.98, 0.82, 0.59$ at $z = 6, 7, 8$.

3. Cross-Correlation Studies

3.1. Cross-Power Spectrum

In this section, I discuss how measurements of the 21 cm and Ly α fluctuation fields are cross-correlated. To make a cross-correlation measurement of the 21 cm and Ly α fluctuation fields, I make use of the power spectrum, a statistical measurement of the variance in fluctuations of some field at different spatial scales. The power spectrum, $P(\mathbf{k})$, is formally defined using the following relationship,

$$\langle \tilde{\delta}_i(\mathbf{k})\tilde{\delta}_j(\mathbf{k}') \rangle = (2\pi)^3 \delta_D(\mathbf{k} - \mathbf{k}') P_{ij}(\mathbf{k}), \quad (21)$$

where $\tilde{\delta}$ is the Fourier transform of some fluctuation field, in this case either 21 cm or Ly α , and δ_D is the Dirac delta function. In practice, the power spectrum can be estimated with the relationship below

$$P_{ij}(k) \approx \frac{\sum_{\mathbf{k} \in k} \tilde{\delta}_i(\mathbf{k})\tilde{\delta}_j(\mathbf{k})}{N_k V} \quad (22)$$

where N_k is the number of modes corresponding to a particular k bin and V is the physical volume of survey. Instead of directly plotting, $P(k)$, it is often common to scale the power spectrum to make its units independent of scale,

$$\tilde{\Delta}_{ij}^2(k) = \frac{k^3}{2\pi^2} P_{ij}(k). \quad (23)$$

The expression above is often referred to as the dimensionless power spectrum. This can then be used to calculate the dimensional power spectrum by scaling the dimensionless power spectrum by the mean of the intensity field $\Delta_{ij}^2 = \bar{I}_i \bar{I}_j \tilde{\Delta}_{ij}^2$. These equations can be used to calculate an auto-power spectrum in the case when δ_i and δ_j are the same fluctuation field

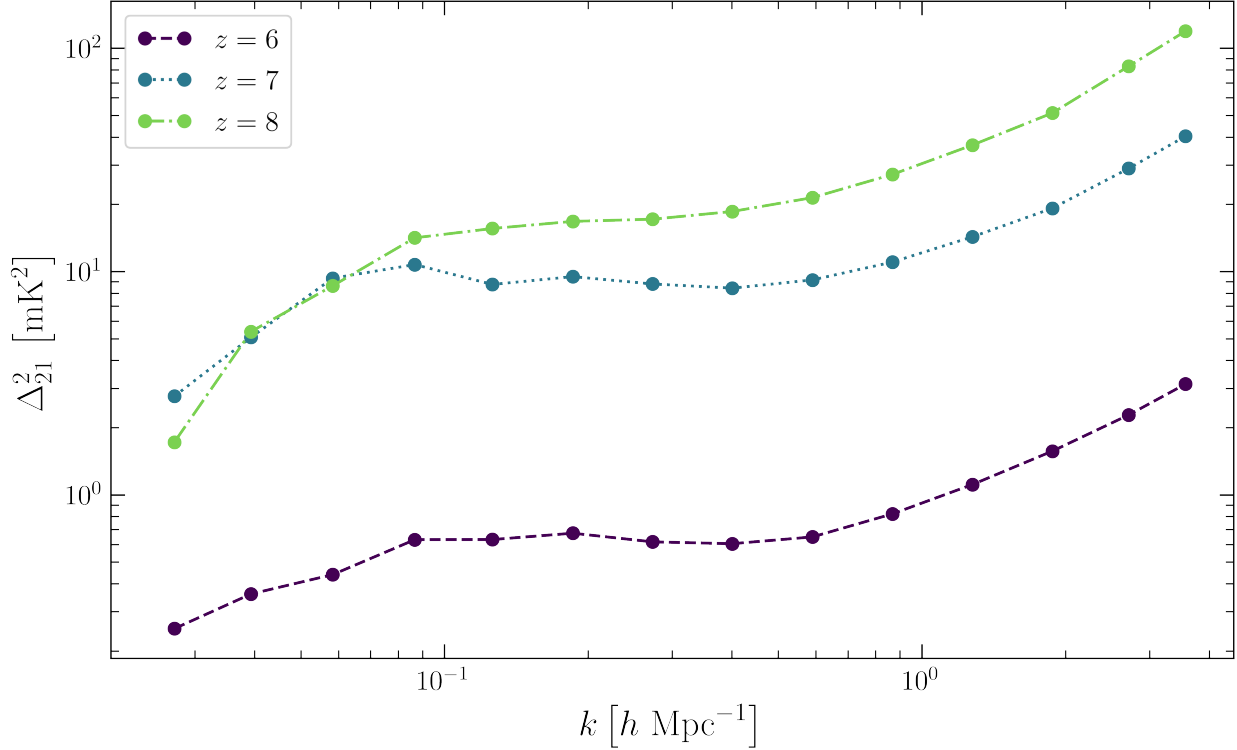


Figure 8. 21 cm power spectra plotted as a function of redshift for the fiducial 21cmFAST model.

or a cross-power spectrum when are they two distinct fields. To calculate the cross-power spectrum, I use these relationships and the 21cm and Ly α fluctuation fields calculated in the previous section. The equations for the 21cm and Ly α auto-power spectra and the 21cm-Ly α cross-power spectrum can be seen below.

$$\Delta_{\text{Ly}\alpha}^2(k) = (\nu \bar{I}_\nu)^2 \tilde{\Delta}_{\text{Ly}\alpha}^2(k) \quad (24)$$

$$\Delta_{21}^2(k) = (\delta \bar{T}_b)^2 \tilde{\Delta}_{21}^2(k) \quad (25)$$

$$\Delta_{21,\text{Ly}\alpha}^2(k) = (\delta \bar{T}_b)(\nu \bar{I}_\nu) \tilde{\Delta}_{21,\text{Ly}\alpha}^2(k) \quad (26)$$

It is important to note that when calculating the cross-power spectrum, Planck's law is used to convert the 21cm brightness temperature, $\delta \bar{T}_b$, to a brightness intensity to simplify the units. The 21cm-Ly α cross-power spectrum is plotted in Figure 10. In this figure, it can be seen that the 21cm-Ly α cross-power spectrum turns-over from positive to negative on at

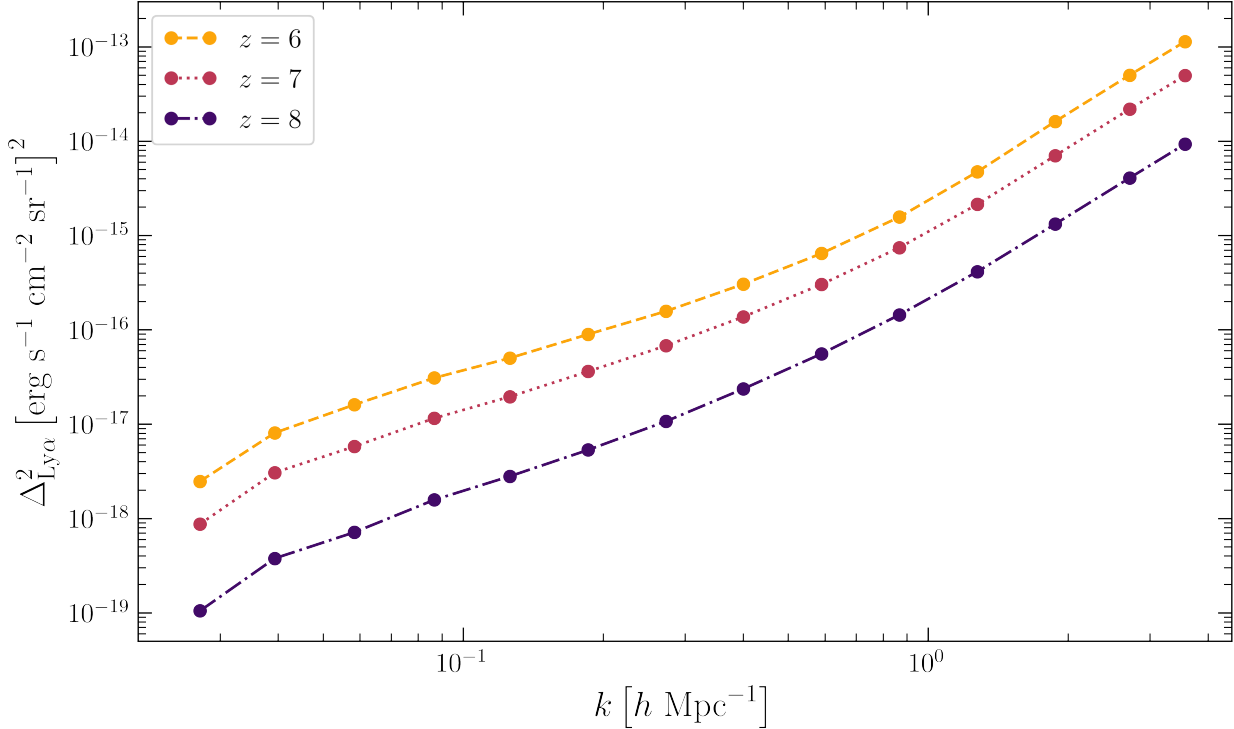


Figure 9. Ly α power spectra plotted for the redshift range of interest. Here, I include the Ly α contributions from both LAE's and the ionized IGM.

each redshifts simulated. This turn-over happens on the scale of the mean ionized bubble size and increases in scale as reionization progresses and the bubbles grow.

I also use the cross-correlation coefficient as an additional metric of understanding the IGM at various scales. This expression is defined as,

$$r(k) = \frac{\Delta_{21, \text{Ly}\alpha}^2(k)}{\sqrt{\Delta_{21}^2(k) \Delta_{\text{Ly}\alpha}^2(k)}}. \quad (27)$$

This relationship expresses how correlated two fluctuation fields are on different scales. For correlated modes, $r(k) > 0$ and for anti-correlated modes $r(k) < 0$. As expected, the cross-correlation coefficient for 21 cm and Ly α measurements (shown in Figure 11) transitions from uncorrelated on small-scales, where the fluctuations from either 21 cm or Ly α emission will be found, to anti-correlated on large-scales, where the fluctuations from the two fields are not overlapping. It is also interesting to note that the cross-correlation coefficient progresses

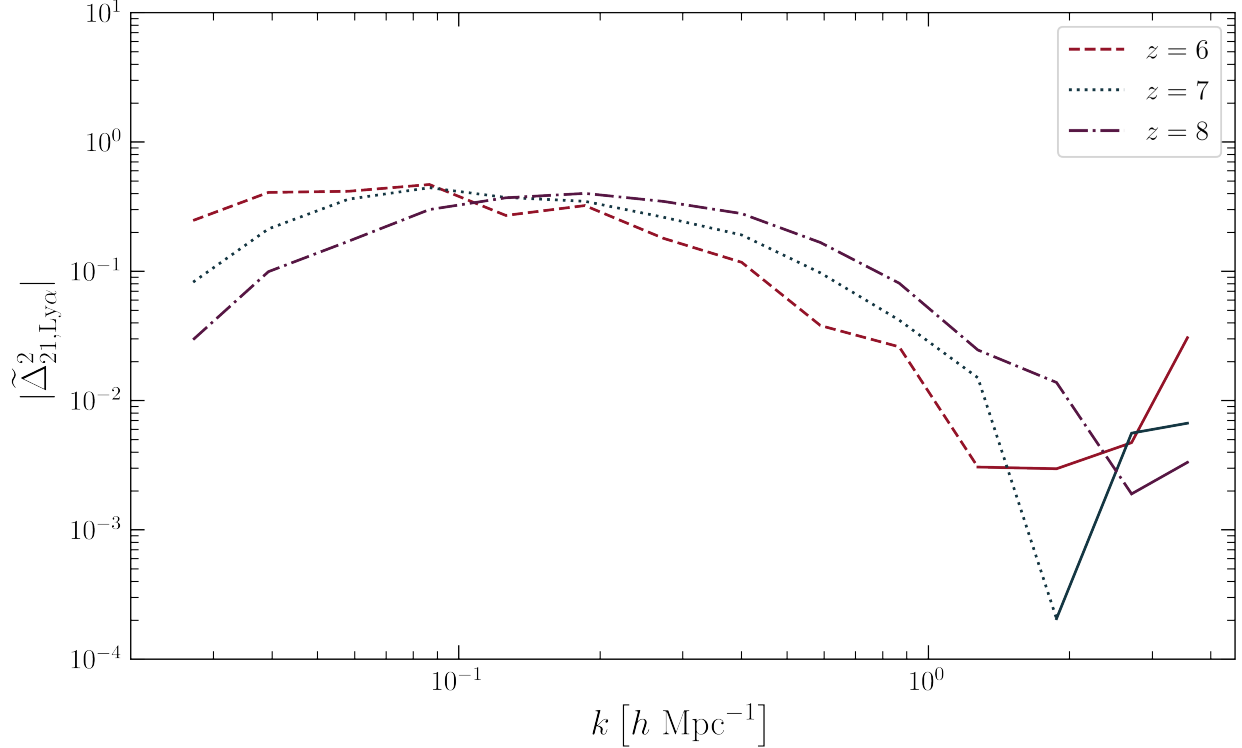


Figure 10. The dimensionless 21 cm-Ly α cross-power spectrum. The solid lines on each of the curves represent positive values in the cross-power spectrum, while varying line styles on the same curves represent negative values. As expected, the cross-power spectrum turns over from positive to negative on the scale of the mean ionized bubble size at that redshift. I also find the cross-power spectrum turns over at increasing scales as reionization progresses, tracing the growth of ionized bubbles.

from generally anti-correlated at high-redshifts to generally uncorrelated towards the end of reionization. This change traces the growth of ionized bubbles through the process of reionization. The scales on which the cross-correlation coefficient transitions from uncorrelated to anti-correlated represents the size of typical ionized bubbles around galaxies.

3.2. Observational Uncertainties

To estimate the feasibility of making a measurement of the 21cm-Ly α cross-power spectrum, it is important to define the sources of uncertainty associated with each measurement. The noise on one particular k -mode in the cross-power spectrum is dependent on noise from both the Ly α and 21 cm measurements, and therefore the uncertainty from both measure-

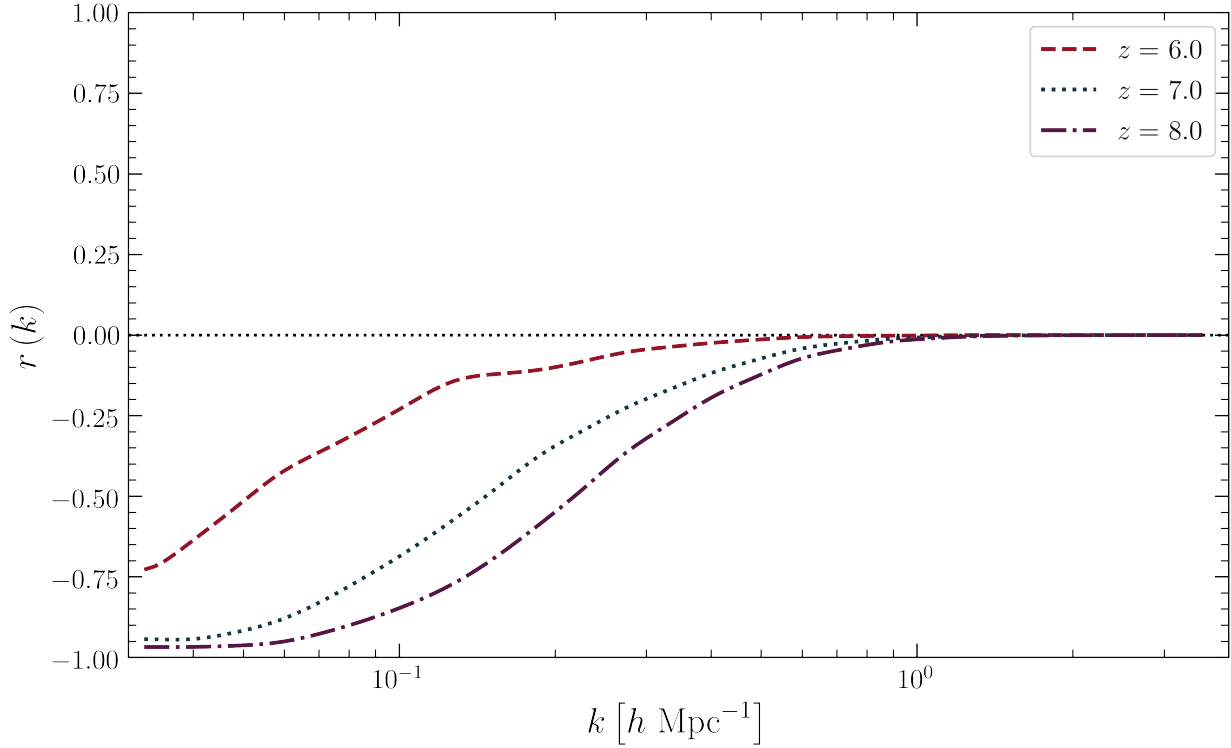


Figure 11. The cross-correlation coefficient (CCC) plotted as a function of scale. Here, a CCC value of -1 indicates that emission of 21 cm and Ly α are completely anti-correlated, while a value of 0 indicates no correlation between emission.

ments must be calculated.

I will begin by discussing the uncertainty associated with 21 cm power spectrum measurements due to sample variance and thermal noise. The total uncertainty associated with an observation of the 21 cm power spectrum can be written as follows,

$$\sigma_{21}(\mathbf{k}) = \left[P_{21}(\mathbf{k}) + P_{21,N}(\mathbf{k}) \right], \quad (28)$$

where P_{21} is the error due to sample variance and $P_{21,N}$ error due to thermal noise variance and is defined as,

$$P_{21,N} = X^2 Y \frac{T_{\text{sys}}^2}{2t} \frac{\Omega_p^2}{\Omega_{\text{pp}}}, \quad (29)$$

where $X^2 Y$ is a scalar term to convert from observed bandwidth and solid angle to k -mode

Table 1: Observing parameters for uncertainty calculations

HERA Observing Parameters	
Observing Days	180
Time Per Day (hrs)	6
Bandwidth (MHz)	8
Dish Size (m)	14
Number of Elements	320
T_{sys} (K)	$100 + 120(\nu/150\text{MHz})^{-2.55}$
SPHEREx Observing Parameters	
$x_{\text{pix}} (\text{''})$	6.2
$\sigma_N [\text{erg s}^{-1} \text{cm}^{-2} \text{sr}^{-1}]$	3×10^{-20}
$V_{\text{vox}} (\text{Mpc}^3)$	0.3
R_{res}	41.5

units, T_{sys} is the system temperature of the array, t is the observation time associated with a particular k -mode, determined by doing the rotation synthesis, Ω_p is the solid angle of the primary beam, and Ω_{pp} is solid angle of the square of the primary beam. More information about the parameters used in this observation can be found in Table 1.

In order to make the calculation of the thermal noise as realistic as possible, I use the method defined in [Pober et al. \(2013\)](#). In this method, uv -coverage of the observation is taken into account using the exact layout of HERA and applying Earth-rotation synthesis to simulate changing uv -bins sampled by each pair of antennas. This uv -coverage then dictates the exact k_{\perp} resolution of the instrument while its spectral resolution sets the k_{\parallel} resolution. I then perform a spherical average over the k_{\parallel} and k_{\perp} bins to identify the observation time, t , associated with each k -bin. Using this observation time, t , and the equation for the thermal noise above a calculation of the 21 cm noise power spectrum can be made.

With the 21 cm noise power spectrum calculated above the uncertainty associated for SPHEREx can then be written similarly to the

$$\sigma_{\text{Ly}\alpha} = [P_{\text{Ly}\alpha} + P_{\text{Ly}\alpha,\text{N}}]. \quad (30)$$

Here $P_{\text{Ly}\alpha}$ represents noise associated with sample variance and $P_{\text{Ly}\alpha,\text{N}}$ represents the thermal

noise variance on a measurement of the Ly α power spectrum and is defined as,

$$P_{\text{Ly}\alpha,\text{N}} = \sigma_{\text{N}}^2 V_{\text{vox}} W_{\text{Ly}\alpha}(k_{\perp}, k_{\parallel}). \quad (31)$$

In the equation above, $\sigma_{\text{N}} = 3 \times 10^{-20}$ erg s $^{-1}$ cm $^{-2}$ sr $^{-1}$ (Doré et al. (2016)) and V_{vox} is volume associated a voxel measured by SPHEREx, set by its angular and spatial resolution. Typically, the thermal noise is defined by just the first two terms, but to account for the limited spectral and spatial resolution of the instrument, the thermal noise is scaled by the window function defined in Lidz et al. (2011),

$$W_{\text{Ly}\alpha}(k_{\perp}, k_{\parallel}) = \exp\left(\left(k_{\perp}/k_{\perp,\text{res}}\right)^2 + \left(k_{\parallel}/k_{\parallel,\text{res}}\right)^2\right). \quad (32)$$

Using, the k_{\perp} and k_{\parallel} values set by HERA baseline lengths and spectral resolution, I calculate the uncertainty on the Ly α power spectrum and spherically average to determine the sensitivity on a particular k -mode. With the both uncertainty on 21 cm and Ly α measurements defined above, the equation for the total variance on the cross-power spectrum can finally be defined using the equation below.

$$\sigma_{21,\text{Ly}\alpha}^2 = \frac{1}{2} [P_{21,\text{Ly}\alpha}^2 + \sigma_{21}\sigma_{\text{Ly}\alpha}] \quad (33)$$

Using the observational treatment and thermal noise errors defined for HERA and SPHEREx defined above and the equation for the error on the cross-power spectrum, the cross-power spectrum error can be calculated by again spherically averaging this 2D noise power spectrum. A plot of the cross-terms in the cross-power spectrum can be found in Figure 12. As can be seen from the figure, the cross-power spectrum, plotted in gray, turns-over on scales that fall below the noise level. While it is encouraging that part of the cross-power spectrum lies above the noise level, ideally a detection of this turn-over would like to be made to place constraints on the typical ionized bubble size surrounding ionizing sources. By identifying

the contributions to the cross-power spectrum error it may be possible to develop observing strategies that make the turn-over detectable.

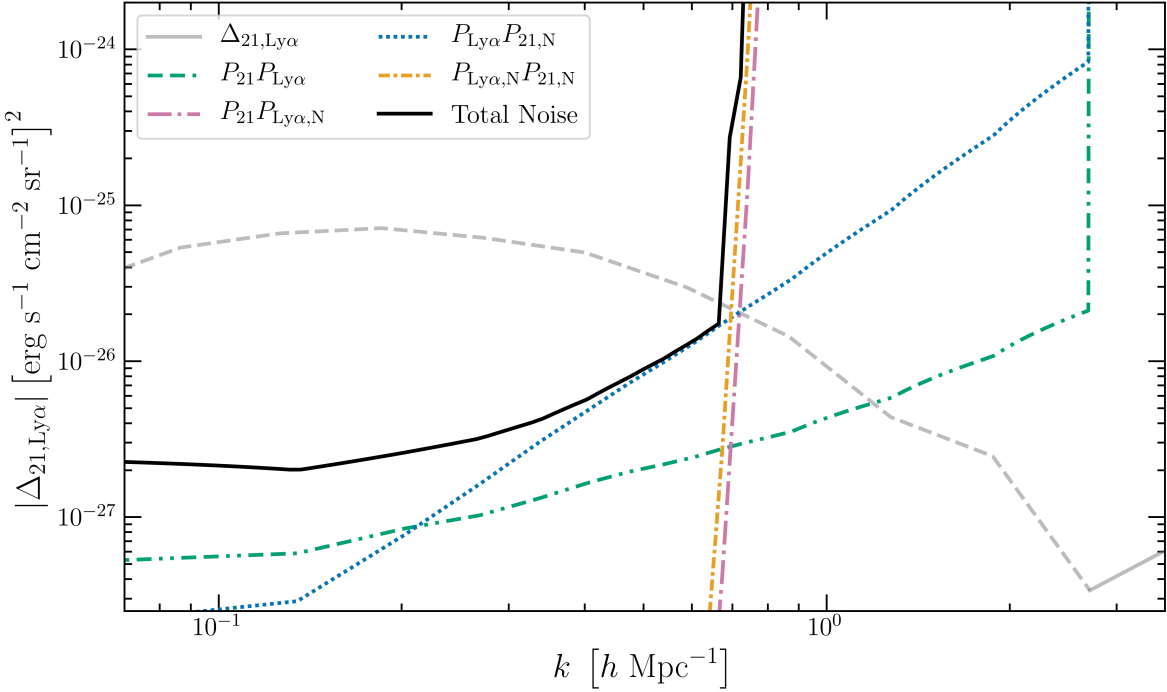


Figure 12. Error budgets of the sensitivity on the cross-power spectrum as measured by HERA and SPHEREx at $z = 8$ when not accounting for the foreground wedge. The terms $P_{21,N}$ and $P_{\text{Ly}\alpha,N}$ represent the thermal noise variance from HERA and SPHEREx respectively. Here, I neglect plotting the cross-power sample variance term, $P_{21,\text{Ly}\alpha}$ as its contribution is negligible, however, it is represented in the total noise of the measurement. For reference, the cross-power spectrum is plotted in gray.

By inspecting Figure 12, it is obvious to see that the dominant sources of error at the scale of the turnover are the $P_{21}P_{\text{Ly}\alpha,N}$ and $P_{21,N}P_{\text{Ly}\alpha,N}$ terms. Because both terms sharply increase at the same scales, it is safe to assume that $P_{\text{Ly}\alpha,N}$, the Ly α thermal noise term, is responsible for the increase due to the window function that accounts for SPHEREx's resolution limitations. This suggests that the feasibility of this measurement is not limited by the thermal noise contributions from either HERA or SPHEREx, but rather limited by SPHEREx's spectral resolution. Because this limitation is a feature of the instrument itself, this tells me that while the cross-power spectrum has the capability of being detected with

a HERA-SPHEREx cross-measurement, the turn-over does not.

3.3. *Foreground Contamination*

Cross-correlation of reionization-era 21 cm observations with Ly α intensity mapping surveys have the advantage that 21 cm foregrounds have no correlation with the low redshift interloper lines that affect high-redshift Ly α measurements. Because the two are uncorrelated, power from the each of these foregrounds is not directly added to the cross-power spectrum. However, while bright foregrounds do not contribute to the amplitude on cross-power spectrum, they do contribute to the total variance on the cross-power spectrum and must be accounted for.

For SPHEREx, the strategy of dealing with foregrounds for EoR measurements is simple: remove voxels whose emission falls above some threshold value ($\sim 1.4 \times 10^{-20}$ W/m 2). Estimates vary on the percentage of pixels that will be masked to cut out near-infrared foregrounds. For now, I assume that the spatial and spectral resolution is SPHEREx is fine enough such that a small percentage of pixels are masked and that the amplitude of the Ly α power spectrum is not significantly changed as a result. Past work estimates that for a SPHEREx-like experiment, roughly 3% of pixels will need to be masked to completely remove foregrounds ([Gong et al. \(2014\)](#)), so it seems like this might be reasonable to assume for now. This may end up being a poor assumption to make and will likely require further investigation to confirm. In the future, I will adopt a method of incorporating pixel masking, such as randomly removing roughly 3% of pixels, to identify its effect on the cross-power spectrum detectability.

For HERA, there are two main strategies to deal with the foregrounds: relying on the fact that the foregrounds are spectrally smooth, and thus confined to an area of the 2D power spectrum known as the foreground wedge, and by precisely modeling foregrounds and subtracting them from the data. There has been some success in subtracting foregrounds from data in other 21 cm experiments, such as with the Murchison Widefield Array ([Barry](#)

et al. (2019)), but because of the difficulty involved with modeling an instrument's response to foregrounds, the primary foreground strategy for HERA will be the removal of the foreground wedge.

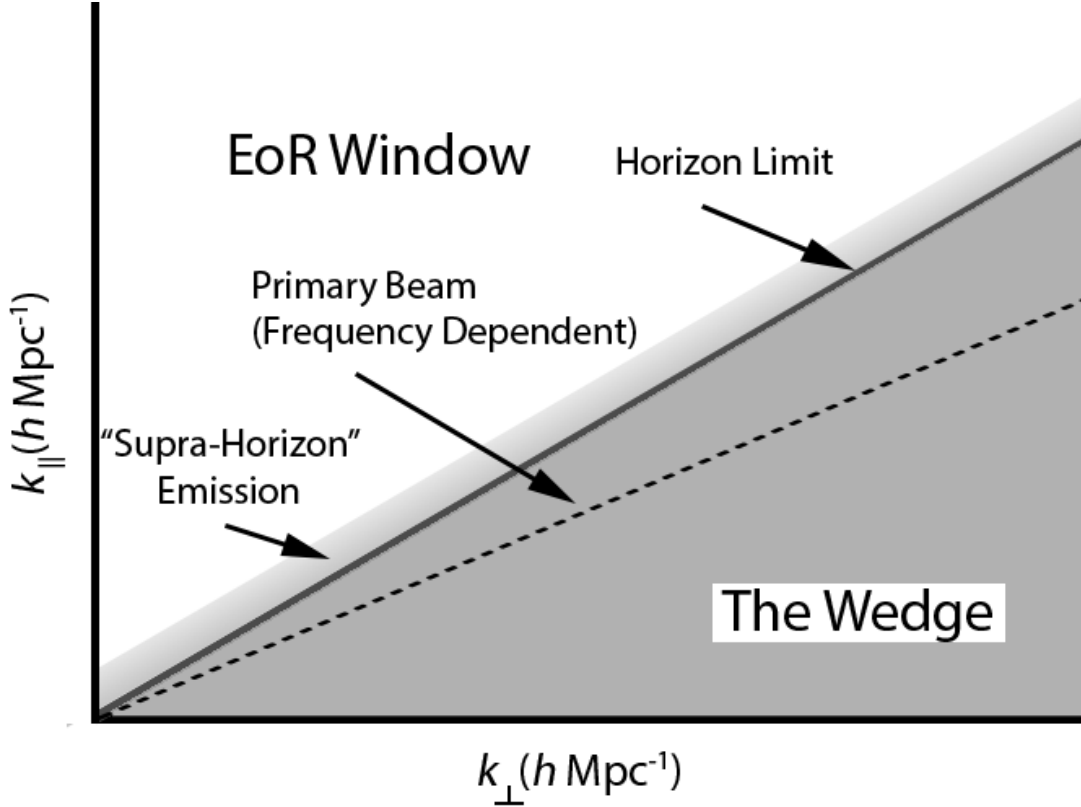


Figure 13. A depiction of the cylindrically averaged 21 cm power spectrum divided into the EoR window and the Wedge. Power from spectrally smooth foregrounds dominate the cosmological 21 cm signal at low k_{\parallel} values and bleed into higher k_{\parallel} modes the further they are from the field center, extending all the way to the horizon in cases of zenith-pointing telescopes such as HERA.

The foreground wedge is a well-documented feature in 21 cm literature (Datta et al. (2010), Morales et al. (2012)) and has been identified as a potential method of removing bright 21 cm foregrounds. To describe it simplistically, that 21 cm foreground wedge is a feature that appears in the cylindrically-averaged 21 cm power spectrum that arises as a result of spectral smooth foregrounds interacting with the chromatic response of an interferometer. Because of their smooth spectral structure, bright foregrounds are defined by lower-order Fourier modes, thus constraining their power to lower k_{\parallel} values. Power from more spectrally

complex 21 cm EoR signal requires higher-order Fourier modes to capture its behavior and is pushed to a region of the 2D power spectrum known as the EoR window as a result. Experiments, such as HERA, have leveraged the fact that the edge of the foreground wedge is dependent on the baseline length of two antennas by building densely packed arrays that sample lower k_{\perp} values, thus increasing the EoR window. The exact relationship defining the k_{\parallel} edge of the wedge can be written as,

$$k_{\parallel,\max} \approx \theta_0 k_{\perp} \frac{D_M(z)}{D_H} \frac{E(z)}{(1+z)}, \quad (34)$$

where θ_0 is the angle between the pointing center and bright foregrounds, k_{\perp} is the Fourier mode dependent on the distance between two dishes, and $k_{\parallel,\max}$ corresponds to the maximum k_{\parallel} value dominated by bright foregrounds. Typically, the safest assumption to make is that $\theta_0 = \pi/2$ which corresponds to bright foregrounds at the horizon, far from the pointing center. In practice, the wedge can extend even beyond the horizon given improperly calibrated chromaticity and mode-mixing effects. Fortunately, there have been results that show contamination from the foregrounds have the potential to be contained within the field of view of the instrument given precise calibration ([Pober et al. \(2014\)](#)).

To investigate the effect of the foreground wedge on the ability to measure the cross-power spectrum, I adopt two treatments of 21 cm foregrounds described in [Pober et al. \(2014\)](#): a moderate foreground treatment, where the foreground wedge extends to the horizon with a horizon buffer added, and an optimistic foreground treatment, where the wedge is confined to the first null in the primary beam of the instrument. In both of these treatments, I remove all samples that fall within the foreground wedge. The effect of the wedge on the 21 cm power spectrum can be observed in Figure 14. For the moderate case, a large number of samples are removed from the data resulting in the thermal noise dominating small k values, while in the optimistic case, many more of those modes are recovered and information on large-scale structure is retained.

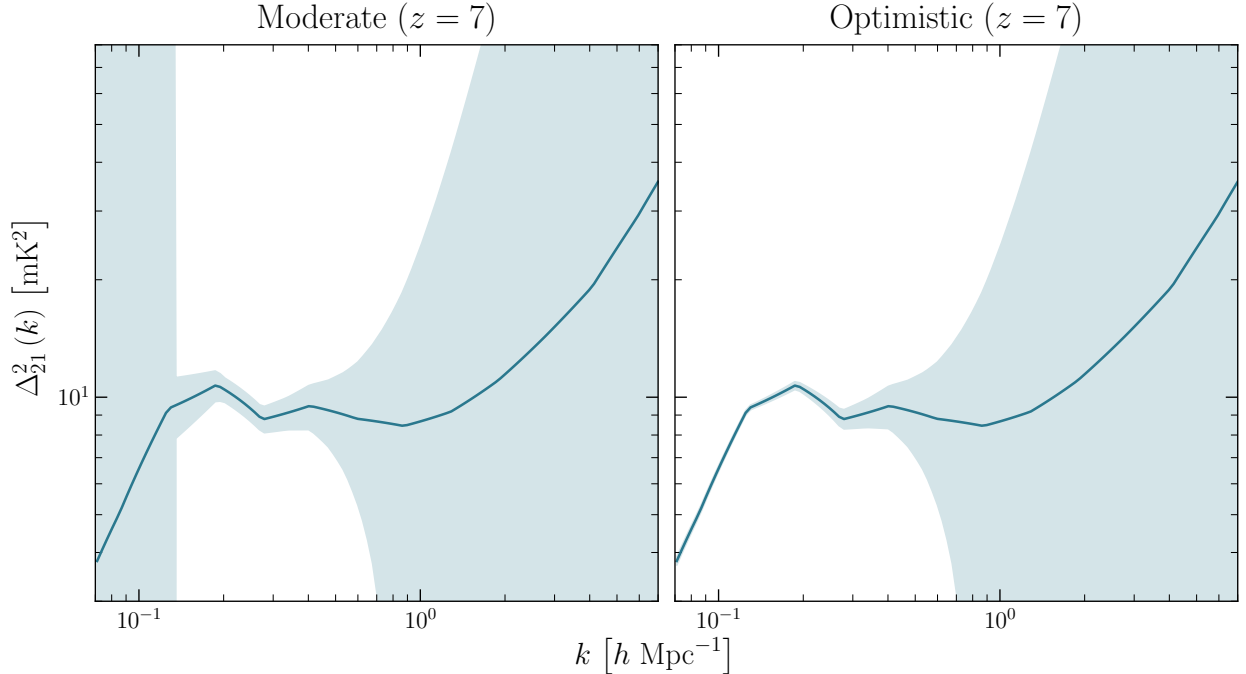


Figure 14. The 21 cm power spectrum plotted with 1σ errors given observing parameters stated in Table 1. Here, I compare the dependence of the two foreground cases on the noise. For the moderate case, all k -modes within the horizon limit are removed resulting in a complete loss of information on large scales $k \lesssim 0.15 h \text{Mpc}^{-1}$. For the optimistic case, foregrounds are confined to the first null in HERA’s beam resulting in a much higher recovery of large scale information.

Propagating these treatments of the 21 cm foregrounds through to the cross-power spectrum, I arrive at the final estimates on the sensitivity of the 21 cm-Ly α cross-power spectrum as measured by HERA and SPHEREx while including thermal noise variance, sample variance, Ly α attenuation, and two treatments of the foreground wedge, shown in Figure 15. While it appears unlikely that a HERA-SPHEREx cross-correlation measurement will be able to measure the cross-power spectrum turn-over, it does appear to be able to make a high sensitivity measurement at large scales, given an optimistic treatment of the foregrounds, and will even be able to make a detection of the cross-power spectrum, assuming a moderate treatment of the foregrounds.

This result gives some confidence in the potential for HERA-SPHEREx synergies in the future. Given even relatively conservative estimates, it seems that these two instruments

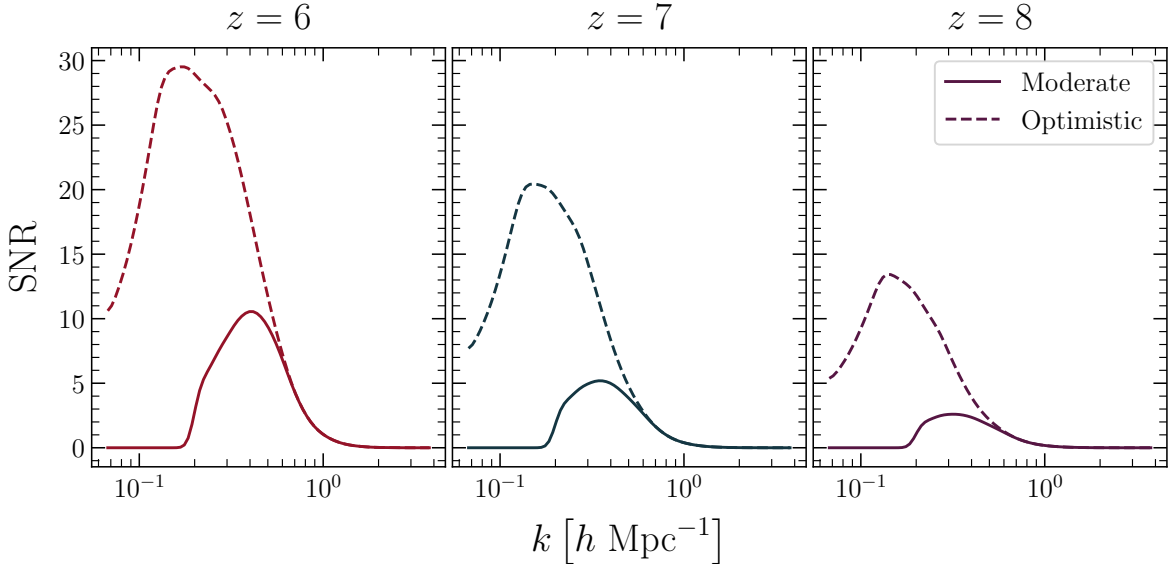


Figure 15. Signal to noise estimates for the 21 cm-Ly α cross-power spectrum. The redshifts $z = [6, 7, 8]$ are plotted for both the optimistic and moderate foreground treatments. These estimates take into account the 21 cm foreground wedge, thermal and sample variance from HERA and SPHEREx, and Ly α attenuation due to absorption in the neutral IGM.

should be able to make a measurement of the cross-power spectrum over their shared redshift range. While past work has shown that the 21 cm-Ly α cross-power spectrum should be a powerful probe of the EoR, it has yet to be seen what information can be extracted from such a measurement with HERA and SPHEREx. The next steps of this work will be to attempt to estimate reionization-era parameters that seem to affect its progression the most through an MCMC analysis. This should give some sense of how useful this metric will be at estimating the underlying physics of reionization.

4. Conclusions

Despite the efforts of first-generation 21 cm experiments and deep galaxy surveys, the Epoch of Reionization remains one of the most mysterious periods in the universe’s history. Next-generation intensity mapping experiments, such as HERA and SPHEREx, look to shed light on this largely unobserved period in our universe’s history. While each instrument should allow for an in-depth study of reionization, synergies between instruments like these will offer independent confirmation on reionization era physics and provide insight on the evolution of the first luminous sources.

While this was a decent proof of concept, a number of potential avenues have the opportunity to be explored in future work to improve its completeness. In Section 3.3, we provided a treatment of 21 cm foregrounds in which, we avoided the foreground dominated region in cylindrically averaged power spectrum by removing all modes within the foreground wedge. In the future, it might be interesting to explore other methods of foreground removal such as foreground subtraction, or a foreground subtraction/avoidance hybrid approach. It is likely that current best levels of foreground modeling and subtraction ([Barry et al. \(2019\)](#)) would dominate the error budget of the cross-power spectrum, but the relatively low noise contribution from SPHEREx may allow the cross-power spectrum to be detectable even in cases of imperfect foreground removal at large scales. In the future, I would like to incorporate this into the analysis to determine its affect on a potential detection.

In addition to Ly α , 21-cm measurements made by HERA will prove to be complementary to intensity mapping measurements of other spectral lines. In particular, instruments measuring the CO(2-1) rotational line (COMAP) and the CII fine-structure line (TIME, CCAT-p, and CONCERTO) will be prime candidates for cross-correlation with HERA in the near future, as the 21-CO and 21-CII cross-power spectra are expected to have a similar

anti-correlation as the 21-Ly α cross-correlation coefficient. One possible extension of this work could be to model intensity mapping from these lines during the EoR using 21cmFAST cubes and estimate the feasibility of HERA of cross-correlating with these experiments given realistic observing strategies. If the 21cm-CO or 21cm-CII cross-power spectrum proves to be measurable, they should each provide additional confirmation of an EoR detection and give insight into ionized bubble size and mean ionization fraction.

Although the cross-power spectrum turn-over will likely remain undetectable by HERA and SPHEREx measurements given these estimates, this detection may still allow for constraints on cosmological and astrophysical parameters. Potentially the most exciting aspect of this cross-correlation work will be determining our ability to break down parameter degeneracies that 21 cm and Ly α measurements are expected to have. In future work, we would like to quantify the accuracy with which the 21cm-Ly α cross-power spectrum can allow us to estimate cosmological parameters. This type of analysis has been done in the past in [Pober et al. \(2014\)](#) with the 21 cm power spectrum and should apply well to this work.

References

- Abel, T., Anninos, P., Zhang, Y., & Norman, M. L. 1997, , 2, 181, doi: [10.1016/S1384-1076\(97\)00010-9](https://doi.org/10.1016/S1384-1076(97)00010-9)
- Alkhidir, T. E., Abdurahman, A., Farhat, I. A. H., et al. 2017, in APS Meeting Abstracts, Vol. 2017, APS March Meeting Abstracts, X42.004
- Barkana, R., & Loeb, A. 2001, PhR, 349, 125, doi: [10.1016/S0370-1573\(01\)00019-9](https://doi.org/10.1016/S0370-1573(01)00019-9)
- Barry, N., Wilensky, M., Trott, C. M., et al. 2019, ApJ, 884, 1, doi: [10.3847/1538-4357/ab40a8](https://doi.org/10.3847/1538-4357/ab40a8)
- Bowman, J. D., Rogers, A. E. E., Monsalve, R. A., Mozdzen, T. J., & Mahesh, N. 2018, Nature, 555, 67, doi: [10.1038/nature25792](https://doi.org/10.1038/nature25792)
- Carucci, I. P., Villaescusa-Navarro, F., & Viel, M. 2017, , 2017, 001, doi: [10.1088/1475-7516/2017/04/001](https://doi.org/10.1088/1475-7516/2017/04/001)
- Chang, T. C., Gong, Y., Santos, M., et al. 2015, in Advancing Astrophysics with the Square Kilometre Array (AASKA14), 4
- Comaschi, P., Yue, B., & Ferrara, A. 2016, MNRAS, 463, 3193, doi: [10.1093/mnras/stw2198](https://doi.org/10.1093/mnras/stw2198)
- Conroy, C., & Wechsler, R. H. 2009, ApJ, 696, 620, doi: [10.1088/0004-637X/696/1/620](https://doi.org/10.1088/0004-637X/696/1/620)
- Curran, S. J., Tzanavaris, P., Darling, J. K., et al. 2010, MNRAS, 402, 35, doi: [10.1111/j.1365-2966.2009.15879.x](https://doi.org/10.1111/j.1365-2966.2009.15879.x)
- Curran, S. J., Tzanavaris, P., Pihlström, Y. M., & Webb, J. K. 2007, MNRAS, 382, 1331, doi: [10.1111/j.1365-2966.2007.12473.x](https://doi.org/10.1111/j.1365-2966.2007.12473.x)
- Datta, A., Bowman, J. D., & Carilli, C. L. 2010, ApJ, 724, 526, doi: [10.1088/0004-637X/724/1/526](https://doi.org/10.1088/0004-637X/724/1/526)

DeBoer, D. R., Parsons, A. R., Aguirre, J. E., et al. 2017, PASP, 129, 045001, doi: [10.1088/1538-3873/129/974/045001](https://doi.org/10.1088/1538-3873/129/974/045001)

Doré, O., Bock, J., Ashby, M., et al. 2014, arXiv e-prints, arXiv:1412.4872. <https://arxiv.org/abs/1412.4872>

Doré, O., Werner, M. W., Ashby, M., et al. 2016, arXiv e-prints, arXiv:1606.07039. <https://arxiv.org/abs/1606.07039>

Dutta, R., Srianand, R., Gupta, N., et al. 2017, MNRAS, 465, 588, doi: [10.1093/mnras/stw2689](https://doi.org/10.1093/mnras/stw2689)

Fan, X., Strauss, M. A., Becker, R. H., et al. 2006, AJ, 132, 117, doi: [10.1086/504836](https://doi.org/10.1086/504836)

Farhat, I. A. H., Alpha, C., Gale, E., et al. 2017a, in APS Meeting Abstracts, Vol. 2017, APS March Meeting Abstracts, Y47.010

Farhat, I. A. H., Gale, E., Alpha, C., & Isakovic, A. F. 2017b, in Journal of Physics Conference Series, Vol. 869, Journal of Physics Conference Series, 012028

Feng, C., Cooray, A., & Keating, B. 2017, ApJ, 846, 21, doi: [10.3847/1538-4357/aa7ff1](https://doi.org/10.3847/1538-4357/aa7ff1)

Furlanetto, S. R., & Lidz, A. 2007, ApJ, 660, 1030, doi: [10.1086/513009](https://doi.org/10.1086/513009)

Furlanetto, S. R., Oh, S. P., & Briggs, F. H. 2006, PhR, 433, 181, doi: [10.1016/j.physrep.2006.08.002](https://doi.org/10.1016/j.physrep.2006.08.002)

Gong, Y., Cooray, A., Silva, M., et al. 2012, in American Astronomical Society Meeting Abstracts, Vol. 219, American Astronomical Society Meeting Abstracts #219, 427.17

Gong, Y., Silva, M., Cooray, A., & Santos, M. G. 2014, ApJ, 785, 72, doi: [10.1088/0004-637X/785/1/72](https://doi.org/10.1088/0004-637X/785/1/72)

Gould, A., & Weinberg, D. H. 1996, ApJ, 468, 462, doi: [10.1086/177707](https://doi.org/10.1086/177707)

Guha Sarkar, T., & Bharadwaj, S. 2011, arXiv e-prints, arXiv:1112.0745. <https://arxiv.org/abs/1112.0745>

—. 2013, , 2013, 023, doi: [10.1088/1475-7516/2013/08/023](https://doi.org/10.1088/1475-7516/2013/08/023)

Guha Sarkar, T., & Bharadwaj, S. 2014, in Journal of Physics Conference Series, Vol. 484, Journal of Physics Conference Series, 012033

Guha Sarkar, T., Bharadwaj, S., Choudhury, T. R., & Datta, K. K. 2011, MNRAS, 410, 1130, doi: [10.1111/j.1365-2966.2010.17509.x](https://doi.org/10.1111/j.1365-2966.2010.17509.x)

Gunn, J. E., & Peterson, B. A. 1965, ApJ, 142, 1633, doi: [10.1086/148444](https://doi.org/10.1086/148444)

Hayes, M., Schaefer, D., Östlin, G., et al. 2011, ApJ, 730, 8, doi: [10.1088/0004-637X/730/1/8](https://doi.org/10.1088/0004-637X/730/1/8)

Heneka, C., Cooray, A., & Feng, C. 2017, ApJ, 848, 52, doi: [10.3847/1538-4357/aa8eed](https://doi.org/10.3847/1538-4357/aa8eed)

Hutter, A., Dayal, P., Müller, V., & Trott, C. M. 2017, ApJ, 836, 176, doi: [10.3847/1538-4357/836/2/176](https://doi.org/10.3847/1538-4357/836/2/176)

Hutter, A., Dayal, P., Partl, A. M., & Müller, V. 2014, MNRAS, 441, 2861, doi: [10.1093/mnras/stu791](https://doi.org/10.1093/mnras/stu791)

Kubota, K., Inoue, A. K., Hasegawa, K., & Takahashi, K. 2019, arXiv e-prints, arXiv:1910.02361. <https://arxiv.org/abs/1910.02361>

Kubota, K., Yoshiura, S., Takahashi, K., et al. 2018, MNRAS, 479, 2754, doi: [10.1093/mnras/sty1471](https://doi.org/10.1093/mnras/sty1471)

Lidz, A., Furlanetto, S. R., Oh, S. P., et al. 2011, ApJ, 741, 70, doi: [10.1088/0004-637X/741/2/70](https://doi.org/10.1088/0004-637X/741/2/70)

Liu, A., & Shaw, J. R. 2019, arXiv e-prints, arXiv:1907.08211. <https://arxiv.org/abs/1907.08211>

Maraston, C. 2005, MNRAS, 362, 799, doi: [10.1111/j.1365-2966.2005.09270.x](https://doi.org/10.1111/j.1365-2966.2005.09270.x)

Mesinger, A., Furlanetto, S., & Cen, R. 2011, MNRAS, 411, 955, doi: [10.1111/j.1365-2966.2010.17731.x](https://doi.org/10.1111/j.1365-2966.2010.17731.x)

Miralda-Escudé, J. 1998, ApJ, 501, 15, doi: [10.1086/305799](https://doi.org/10.1086/305799)

Morales, M. F., Hazelton, B., Sullivan, I., & Beardsley, A. 2012, ApJ, 752, 137, doi: [10.1088/0004-637X/752/2/137](https://doi.org/10.1088/0004-637X/752/2/137)

Neben, A. R., Stalder, B., Hewitt, J. N., & Tonry, J. L. 2017, ApJ, 849, 50, doi: [10.3847/1538-4357/aa8f9c](https://doi.org/10.3847/1538-4357/aa8f9c)

Parsons, A. R., Backer, D. C., Foster, G. S., et al. 2010, AJ, 139, 1468, doi: [10.1088/0004-6256/139/4/1468](https://doi.org/10.1088/0004-6256/139/4/1468)

Planck Collaboration, Ade, P. A. R., Aghanim, N., et al. 2016, A&A, 594, A13, doi: [10.1051/0004-6361/201525830](https://doi.org/10.1051/0004-6361/201525830)

Pober, J. C., Parsons, A. R., DeBoer, D. R., et al. 2013, AJ, 145, 65, doi: [10.1088/0004-6256/145/3/65](https://doi.org/10.1088/0004-6256/145/3/65)

Pober, J. C., Liu, A., Dillon, J. S., et al. 2014, ApJ, 782, 66, doi: [10.1088/0004-637X/782/2/66](https://doi.org/10.1088/0004-637X/782/2/66)

Pritchard, J. R., & Furlanetto, S. R. 2007, MNRAS, 376, 1680, doi: [10.1111/j.1365-2966.2007.11519.x](https://doi.org/10.1111/j.1365-2966.2007.11519.x)

Pullen, A. R., Doré, O., & Bock, J. 2014, ApJ, 786, 111, doi: [10.1088/0004-637X/786/2/111](https://doi.org/10.1088/0004-637X/786/2/111)

Razoumov, A. O., & Sommer-Larsen, J. 2010, ApJ, 710, 1239, doi: [10.1088/0004-637X/710/2/1239](https://doi.org/10.1088/0004-637X/710/2/1239)

Santos, M. G., Amblard, A., Pritchard, J., et al. 2008, ApJ, 689, 1, doi: [10.1086/592487](https://doi.org/10.1086/592487)

Sarkar, T. G., Datta, K. K., Pal, A. K., Choudhury, T. R., & Bharadwaj, S. 2016, Journal of Astrophysics and Astronomy, 37, 26, doi: [10.1007/s12036-016-9404-y](https://doi.org/10.1007/s12036-016-9404-y)

Sarkar, T. G., & Sen, A. A. 2016, Journal of Astrophysics and Astronomy, 37, 33, doi: [10.1007/s12036-016-9407-8](https://doi.org/10.1007/s12036-016-9407-8)

Schaerer, D. 2002, A&A, 382, 28, doi: [10.1051/0004-6361:20011619](https://doi.org/10.1051/0004-6361:20011619)

Silva, M. B., Santos, M. G., Gong, Y., Cooray, A., & Bock, J. 2013, ApJ, 763, 132, doi: [10.1088/0004-637X/763/2/132](https://doi.org/10.1088/0004-637X/763/2/132)

Silva, M. B., & Zaroubi, S. 2018, in IAU Symposium, Vol. 333, Peering towards Cosmic Dawn, ed. V. Jelić & T. van der Hulst, 250–253

Slosar, A., Cooray, A., & Silk, J. I. 2007, MNRAS, 377, 168, doi: [10.1111/j.1365-2966.2007.11584.x](https://doi.org/10.1111/j.1365-2966.2007.11584.x)

Sobacchi, E., Mesinger, A., & Greig, B. 2016, MNRAS, 459, 2741, doi: [10.1093/mnras/stw811](https://doi.org/10.1093/mnras/stw811)

Sun, G., Hensley, B. S., Chang, T.-C., Doré, O., & Serra, P. 2019, arXiv e-prints, arXiv:1907.02999. <https://arxiv.org/abs/1907.02999>

Teymourzadeh, R., Alpha, A., & Mok, V. 2018, arXiv e-prints, arXiv:1806.04576. <https://arxiv.org/abs/1806.04576>

Tingay, S. J., Goeke, R., Bowman, J. D., et al. 2013, PASA, 30, e007, doi: [10.1017/pasa.2012.007](https://doi.org/10.1017/pasa.2012.007)

Visbal, E., & McQuinn, M. 2018, ApJL, 863, L6, doi: [10.3847/2041-8213/aad5e6](https://doi.org/10.3847/2041-8213/aad5e6)

Whitler, L. R., Mason, C. A., Ren, K., et al. 2019, arXiv e-prints, arXiv:1911.03499. <https://arxiv.org/abs/1911.03499>

Yatawatta, S., de Bruyn, A. G., Brentjens, M. A., et al. 2013, A&A, 550, A136, doi: [10.1051/0004-6361/201220874](https://doi.org/10.1051/0004-6361/201220874)

Zhang, J. 2006, PhD thesis, Columbia University